crystal families in space E^o, as explained in §II [see Table 2(*f*)].

Splitting $E^6 = E^3 \oplus E^1 \oplus E^1 \oplus E^1$. There are two gZ-irr. crystal families in space E^3 and one in space E^1, which generate two gZ-red. crystal families in space E^6 because the splitting $E^1 \oplus E^1 \oplus E^1$ only generates the orthorhombic crystal family [see Table 2(*g*)].

Splitting $E^6 = E^2 \oplus E^2 \oplus E^1 \oplus E^1$. There are three gZ-irr. crystal families in space E^2 and one in space E^1 which generate six gZ-red. crystal families in space E^6. Indeed, the splitting $E^2 \oplus E^2$ generates six crystal families, six being the number of combinations with repetitions of three elements taken two at a time, whereas the splitting $E^1 \oplus E^1$ only generates the rectangular crystal family [see Table 2(*h*)].

Splitting $E^6 = E^2 \oplus E^1 \oplus E^1 \oplus E^1 \oplus E^1$. There are three gZ-ir. crystal families in space E^2 and one in space E^1. The splitting $E^1 \oplus E^1 \oplus E^1 \oplus E^1$ only generates the orthotopic 4 crystal family; therefore, we obtain three gZ-red. crystal families in space E^6 [see Table 2(*i*)].

Splitting $E^6 = E^1 \oplus E^1 \oplus E^1 \oplus E^1 \oplus E^1 \oplus E^1$. This splitting generates the orthotopic 6 crystal family of space E^6 [see Table 2(*j*)].

Concluding remarks

The geometrical method that introduced by Veysseyre *et al.* (1993) and Weigel & Vesseyre (1993) is a convenient and powerful means to construct all the gZ-red. crystal families of space E^n; this method enables us to describe the cell of the crystal family and to give a name to this family as well as a symbol to its holohedry. Moreover, we can summarize the previous results by mentioning the number of crystal families belonging to each type of splitting of space E^6. This enables us to prove the results given in Table 3 of Weigel & Veysseyre (1993).

References

PHAN, T., VEYSSEYRE, R. & WEIGEL, D. (1988). *Acta Cryst.* A**44**, 627–637.
PLESKEN, W. & HANRATH, W. (1984). *Math. Comput.* **43**, 573–587.
VEYSSEYRE, R., WEIGEL, D. & PHAN, T. (1993). *Acta Cryst.* A**49**, 481–486.
WEIGEL, D., PHAN, T. & VEYSSEYRE, R. (1987). *Acta Cryst.* A**43**, 294–304.
WEIGEL, D. & VEYSSEYRE, R. (1993). *Acta Cryst.* A**49**, 486–492.
WEIGEL, D. & VEYSSEYRE, R. (1994). *Acta Cryst.* A**50**, 444–450.

Acta Cryst. (1995). A**51**, 134–142

Heights and Widths of *Umweganregung* Profiles in Comparison with Bragg Reflection Profiles

By ELISABETH ROSSMANITH AND KAI BENGEL

Mineralogisch-Petrographisches Institut der Universität Hamburg, D-20146 Hamburg, Grindelallee 48, Germany

(*Received* 14 *March* 1994; *accepted* 14 *July* 1994)

Abstract

The excellent agreement between experimental *Umweganregung* patterns and those calculated with *UMWEG*90 [Rossmanith (1992). *Acta Cryst.* A**48**, 596–610] has been demonstrated by Rossmanith, Adiwidjaja, Eck, Kumpat & Ulrich [*J. Appl. Cryst.* (1994), **27**, 510–516]. It has also been shown that, by fitting calculated to experimental ψ scans, consistent and physically significant parameters for the mosaic-structure parameters of the sample – mosaic spread and mosaic-block size – and for the divergence parameter of the X-ray beam can be obtained. In this paper, it is shown that, furthermore, the relative intensities of ψ scans of different forbidden reflections of a particular sample are predicted satisfactorily with *UMWEG*90 using the parameters obtained in the previously mentioned paper. To make an appraisal of the possible maximum gain due to *Umweganregung*, ω–2θ–ψ scans of 14 forbidden reflections of a particular zinc sample were analysed. By comparison of the ω–2θ intensity profiles and integrated intensities of the multiple diffraction events with those of the rocking curves of 15 Bragg reflections with neighbouring Bragg angles, the statements given in standard textbooks, that the profiles of *Umweganregung* events are much sharper and the intensities much smaller than those of possible Bragg reflections, are disproved.

Introduction

For the determination of distortions of atomic charge densities from spherical symmetry due to anharmonic motion and chemical bonding, very weak 'almost forbidden' as well as weak high-order Bragg reflections have to be measured. These weak intensities may be

systematically increased by multiple diffraction, falsifying the results of exact charge-density determination. For an exact analysis, it is therefore important to know the intensity gain of the very weak Bragg intensity caused by the *Umweganregung* effect. As far as the authors know, until now there has not been available any generally valid correction algorithm for this effect. A first approach to such a correction is given by the program *UMWEG*90 (Rossmanith, 1992), with which a simulation of ψ scans can be calculated in the framework of the kinematical theory.

The excellent agreement between experimental *Umweganregung* patterns and those calculated with *UMWEG*90 has been demonstrated by Rossmanith, Adiwidjaja, Eck, Kumpat & Ulrich (1994). It has been shown that consistent and physically significant parameters can be obtained for the mosaic-structure parameters of the sample – mosaic spread η and mosaic-block radius r – and for the divergence parameter of the X-ray beam by fitting calculated to experimental ψ scans.

In this paper, the intensities calculated with *UMWEG*90 are compared with experimental multiple diffraction intensities of 14 forbidden reflections of one particular zinc sample, measured in a θ range between about 9 and 45°. It is shown that the relative intensities as well as both widths, that of the ω–2θ-scan profiles, $\Delta\theta$, and that of ψ-scan profiles, $\Delta\psi$, of these 14 forbidden reflections are predicted satisfactorily with *UMWEG*90 using the parameter set obtained by Rossmanith *et al.* (1994).

On the other hand, the identification of space-group extinctions is sometimes confounded by the presence of multiple-diffraction events. The second aim of this paper is to check the statement given in standard textbooks, that the multiple-diffraction ω-scan profiles observed for the forbidden reflections should easily be distinguishable from single Bragg reflections because of their different shape. [Azaroff (1968) states 'Because of the more regular shape of such double reflections, they can be identified when photographic recording of intensities is employed, so that they should not cause confusion in spacegroup determination.'; Lipson & Cochran (1957) state 'The double reflections can, however, be recognized by their shapes; since they are formed by reflexion of truly parallel rays, they are much sharper than ordinary spots, and so cannot easily be mistaken for them.'] The profiles and especially the half-widths of the measured ω–2θ scans of multiple-diffraction events are therefore compared with the profiles of Bragg reflections measured in the equivalent θ range as well as with theoretical half-widths also obtained with *UMWEG*90.

Experimental

For the measurements of the single- and multiple-diffraction events, a zinc single-crystal sphere with diameter $D = 100\,\mu m$ was used. Zinc crystallizes in the hexagonal-close-packed (h.c.p.) space group $P6_3/mmc$ (No. 194) with two atoms per unit cell ($a = 2.664$, $c = 4.937$ Å) in the special position $\pm\frac{1}{3},\frac{2}{3},\frac{1}{4}$ (anisotropic temperature parameters: $\beta_{11} = \beta_{22} = 0.03796$, $\beta_{33} = 0.02061$, $\beta_{12} = \beta_{11}/2$, $\beta_{13} = \beta_{23} = 0$), resulting in the conditions limiting possible reflections: hhl, $l = 2n$ (general) and $h - k = 3n$, $l = 2n$ (special).

The experiment was performed on the Enraf–Nonius CAD-4 diffractometer using Ag $K\alpha$ radiation. The 002 reflection of a graphite single crystal was used for monochromatization of the primary X-ray beam. In conventional experiments, the intensity of the Bragg reflections, *i.e.* the intensity recorded during an ω–2θ scan, is measured at the azimuthal angle $\psi = 0$, defined by the CAD-4 software. This intensity may be enlarged or diminished by multiple-scattering events.

In the case of forbidden reflections, only an intensity gain by *Umweganregung* is possible. With *UMWEG*90, which makes possible the simulation of ψ scans, the intensity due to *Umweganregung* events in the neighbourhood of the azimuthal angle $\psi = 0$ can be calculated when the orientation matrix is known (Rossmanith, Kumpat & Schulz, 1990).

To make an appraisal of the possible intensity gain at $\psi = 0°$, the ψ scans of the forbidden reflections with Bragg angles $\psi < 45°$ were calculated. 14 of these forbidden reflections, with significant theoretical intensity in the vicinity of $\psi = 0°$, almost uniformly spread over the θ range in consideration, were chosen for measurement. For these 14 forbidden reflections, *Umweganregung* patterns were recorded in the ω–2θ–ψ-scan technique. In this technique, for each of the 150 equidistant azimuthal angles ψ in the range between $\psi = -1.5$ and $\psi = 1.5°$, the intensity is measured in an ω–2θ scan with a scan width in θ equal to 0.725°. The 10 min measuring time for each ω–2θ scan per 0.02° ψ step was chosen to guarantee that the standard deviations $\sigma(I)$ of the individual integrated intensities $I(\psi_i)$ were less than ~ 1% of these intensities even in the low-intensity region. In Fig. 1, the three-dimensional plot of the ω–2θ–ψ scan of the forbidden $0\bar{3}3$ reflection is shown as an example.

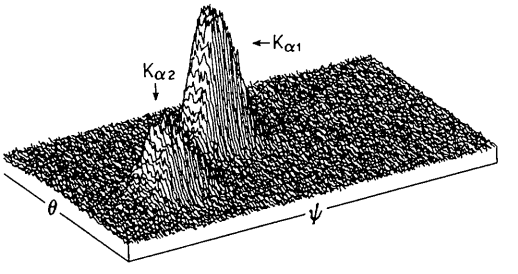

Fig. 1. Three-dimensional plot of the ω–2θ–ψ scan of the forbidden $0\bar{3}3$ reflection. Intensity *versus* Bragg angle θ and azimuthal angle ψ.

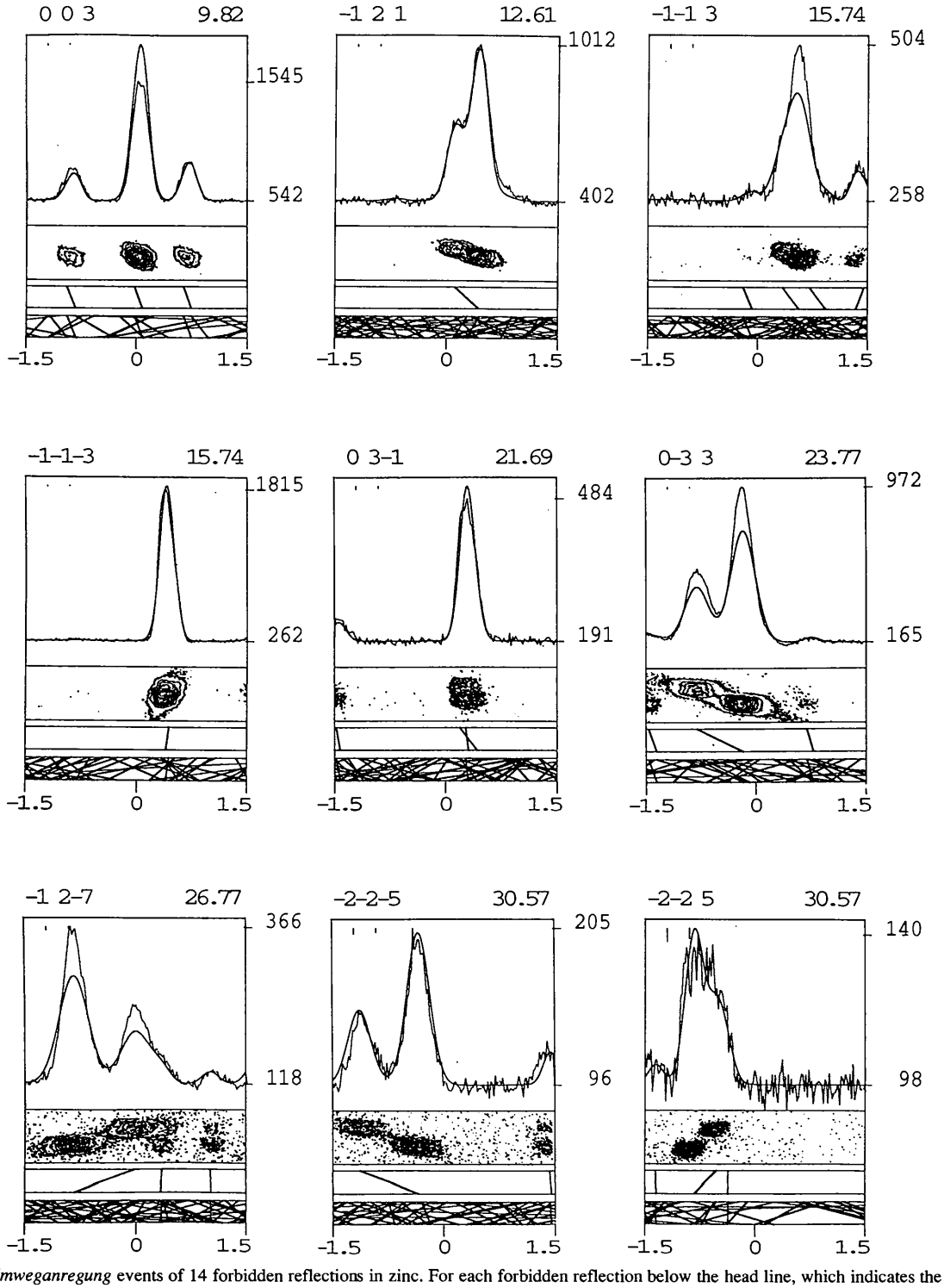

Fig. 2. *Umweganregung* events of 14 forbidden reflections in zinc. For each forbidden reflection below the head line, which indicates the indices and the mean Bragg angle, $(\theta_{K\alpha_1} + \theta_{K\alpha_2})/2$, of the forbidden reflection, four diagrams are given: From bottom to top: (i) *Umweganregung*-peak-location plot (λ–ψ diagram) representing the peak location lines of all *Umweganregung* events in the wavelength range Ag $K\alpha_1 < \lambda <$ Ag $K\alpha_2$ (ordinate) and the ψ range ±1.5° (abscissa). (ii) *Umweganregung*-peak-location plot (λ–ψ diagram), as before, but with only the most intense lines, which mainly contribute to the measured *Umweganregung* peaks, selected. Indices, intensities and ψ values of these lines are given in Table 1. (iii) Contour plot of the measurement. $\omega/2\theta$-scan range = 0.725° (ordinate) *versus* ±1.5°ψ range (abscissa). The lowest contour corresponds to 1.6 times the background intensity. (iv) Experimental (dashed lines) and theoretical (solid lines) *Umweganregung* patterns of the 14 forbidden reflections. The two intensity values given at the right border of this diagram correspond to the background intensity integrated over the ω–2θ scan and the maximum measured integrated intensity (counts min^{-1}) of the pattern.

For comparison of the ω–2θ intensity profiles caused by *Umweganregung* with those of the permitted Bragg reflections, 15 permitted reflections were measured in the range $\theta < 45°$ in the ω–2θ scanning technique.

Comparison of experimental and calculated *Umweganregung* patterns of forbidden reflections

In Fig. 2, four diagrams are given for each of the 14 forbidden reflections. The *Umweganregung*-peak-location plot (λ–ψ diagram) given in the lowest diagram corresponding to each particular forbidden reflection shows the peak-location lines of all *Umweganregung* events in the wavelength range Ag $K\alpha_1 < \lambda <$ Ag $K\alpha_2$ (ordinate) and azimuthal angle range $-1.5 < \psi < 1.5°$ (abscissa). In the second λ–ψ diagram, lying on top of the first, only the lines, which mainly contribute to the measured *Umweganregung* peaks (see Table 1 for indices, intensities and ψ values of these lines), were selected. Above the two λ–ψ diagrams, the contour plot of the measurement is given in the correct θ-range (ordinate, 0.725°) to ψ-range (abscissa, ±1.5) proportion. The experimental *Umweganregung* patterns given by the dashed lines in the uppermost diagram are obtained by plotting the integrated intensities over the ω–2θ scans (ordinate: intensity in counts min^{-1}) against ψ. The two intensity values given at the right border of this diagram correspond to the background intensity integrated over the ω–2θ scan and the maximum measured integrated intensity [counts min^{-1}] of the respective pattern. The two error bars in the upper left corner of each *Umweganregung* pattern represent the standard deviations of the maximum and minimum integrated intensity of the measured pattern, respectively. In the heading of the four diagrams, the indices and the Bragg angle of the respective forbidden reflection are given.

In the intensity-*versus*-ψ diagrams of Fig. 2, the measured *Umweganregung* patterns (dashed lines) are compared with the simulations calculated with *UMWEG*90 (solid lines) using the parameter set obtained for Ag $K\alpha$ radiation by Rossmanith *et al.*

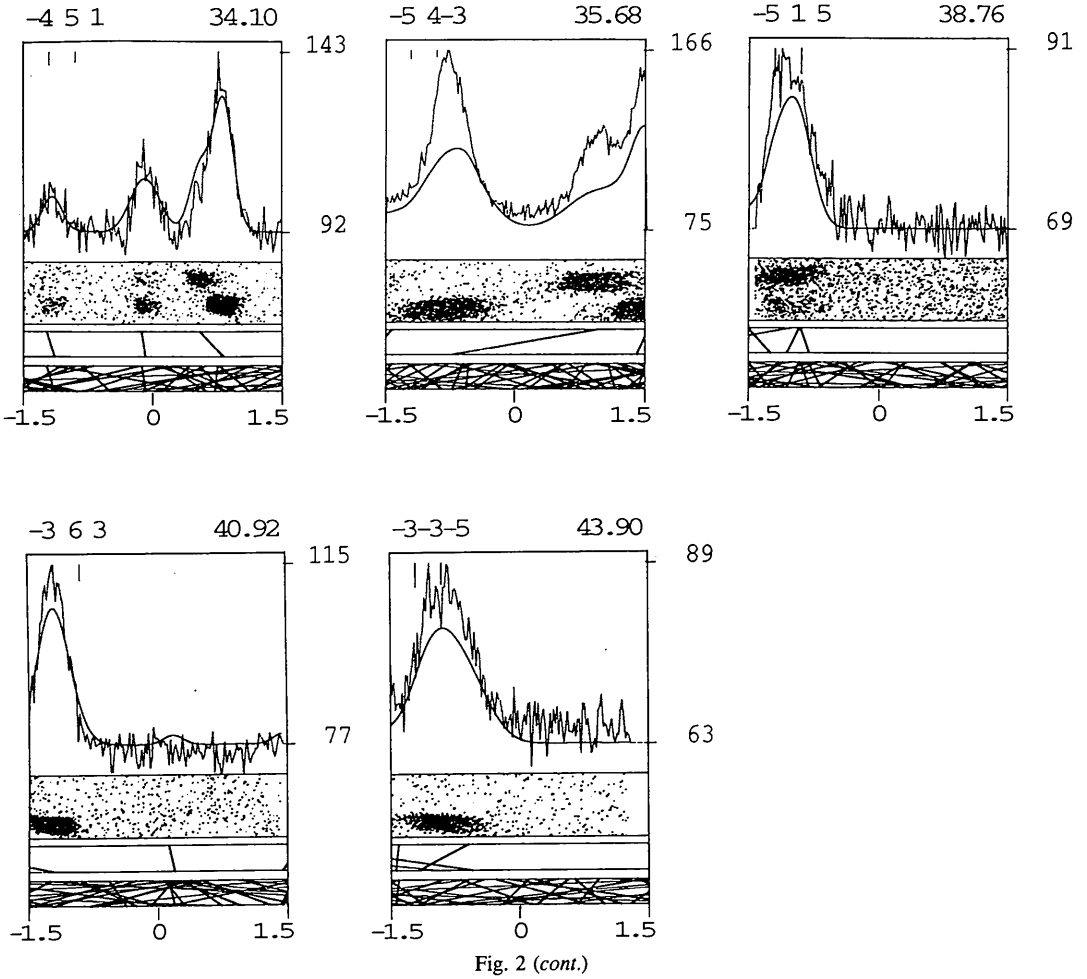

Fig. 2 (*cont.*)

Table 1. *Miller indices of the primary, operative and cooperative reflections, intensities and ψ values for the two characteristic lines of the Umweganregung events mainly contributing to the measured Umweganregung peaks*

Intensities are given as percentages; 100% corresponds to the most intense event in the 360° ψ scan.

hkl	$(hkl)_{op}$	$(hkl)_{coop}$	I (%)	$\psi_{K\alpha_1}$ (°)	$\psi_{K\alpha_2}$ (°)
003	$0\bar{2}0$	023	5.7	−0.83	−0.95
	$0\bar{2}\bar{3}$	020	5.4	−0.83	−0.95
	$0\bar{1}\bar{1}$	014	32.8	0.09	−0.02
	$0\bar{1}4$	$01\bar{1}$	28.1	0.09	−0.02
	$0\bar{2}1$	022	7.7	0.76	0.65
	$0\bar{2}\bar{2}$	021	7.6	0.76	0.65
$\bar{1}21$	$0\bar{1}0$	$\bar{1}31$	18.8	0.44	0.11
$\bar{1}\bar{1}3$	$1\bar{3}\bar{1}$	$\bar{2}24$	0.7	−0.07	−0.20
	$\bar{1}\bar{2}\bar{3}$	010	8.8	0.57	0.34
	$1\bar{1}\bar{3}$	$\bar{2}06$	0.8	0.94	0.71
	$\bar{2}21$	$1\bar{3}2$	2.3	1.35	1.46
$\bar{1}\bar{1}\bar{3}$	$\bar{1}1\bar{3}$	$0\bar{2}0$	10.8	0.40	0.44
	$0\bar{1}0$	$\bar{1}0\bar{3}$	55.5	0.40	0.44
$03\bar{1}$	211	$\bar{2}2\bar{2}$	2.1	−1.42	−1.47
	$\bar{1}1\bar{1}$	120	16.5	0.31	0.27
	$1\bar{1}2$	$\bar{1}4\bar{3}$	1.7	0.42	0.19
$0\bar{3}3$	$1\bar{4}1$	$\bar{1}12$	3.7	−1.35	−1.46
	$0\bar{1}2$	$0\bar{2}1$	100.0	−0.17	−0.80
	$1\bar{1}\bar{2}$	$\bar{1}\bar{2}5$	3.1	0.78	0.69
$\bar{1}2\bar{7}$	$\bar{1}1\bar{4}$	$01\bar{3}$	90.9	−0.84	0.00
	$13\bar{5}$	$0\bar{1}\bar{2}$	6.8	0.34	0.36
	$\bar{1}3\bar{4}$	$0\bar{1}\bar{3}$	7.0	1.02	1.02
$\bar{2}\bar{2}\bar{5}$	$\bar{1}0\bar{1}$	$\bar{1}\bar{2}\bar{4}$	94.4	−0.33	−1.13
	$\bar{1}1\bar{2}$	$\bar{1}\bar{3}\bar{3}$	13.4	1.45	1.43
$\bar{2}\bar{2}5$	$1\bar{3}1$	$\bar{3}14$	3.3	−1.35	−1.35
	$0\bar{2}3$	$\bar{2}02$	36.4	−0.84	−0.52
	$\bar{3}14$	$1\bar{3}1$	3.1	−0.37	−0.37
$\bar{4}51$	$02\bar{1}$	$\bar{4}32$	11.1	−1.14	−1.24
	$\bar{3}50$	$\bar{1}01$	15.6	−0.08	−0.13
	010	$\bar{4}41$	55.1	0.83	0.56
$\bar{5}4\bar{3}$	$\bar{3}10$	$\bar{2}33$	12.4	–	−1.42
	$43\bar{1}$	$\bar{1}12$	58.4	−0.72	0.98
	$\bar{2}00$	$\bar{3}4\bar{3}$	9.0	1.41	–
$\bar{5}15$	$\bar{2}22$	$\bar{3}\bar{1}3$	16.7	−1.24	–
	$\bar{1}03$	$\bar{4}12$	100.0	–	−1.00
	$\bar{3}\bar{1}5$	$\bar{2}20$	6.8	−1.06	−0.91
	$\bar{4}33$	$\bar{1}\bar{2}2$	4.8	−0.80	−0.90
$\bar{3}63$	$\bar{1}42$	$\bar{2}21$	73.9	−1.22	–
	021	$\bar{3}42$	100.0	−1.22	–
	$\bar{1}03$	$\bar{2}60$	7.9	0.19	0.12
	$\bar{1}14$	$\bar{2}5\bar{1}$	12.3	1.45	–
$\bar{3}\bar{3}\bar{5}$	$\bar{2}4\bar{3}$	$\bar{1}1\bar{2}$	8.1	−1.44	−1.41
	$\bar{1}\bar{2}1$	$\bar{2}\bar{1}\bar{6}$	10.2	−1.17	−0.59
	$\bar{1}00$	$\bar{2}\bar{3}\bar{5}$	100.0	−0.93	–
	$3\bar{1}\bar{2}$	$0\bar{2}\bar{3}$	49.3	−0.54	–

(1994), *i.e.* δ_s (the divergence perpendicular to the scattering plane of the primary reflection) is 0.16°, δ_p (the divergence parallel to this plane) is 0.14°, r (the mosaic-block size) is 0.23 μm and η (the mosaic spread) is 0.01°. For the wavelength spread $\Delta\lambda/\lambda$, the half-widths of the characteristic lines of silver [$K\alpha_1$: 0.00048; $K\alpha_2$: 0.00052 (Compton & Allison, 1935)] are used in *UMWEG*90. All the theoretical patterns were calculated with the same constant scale factor 'scal'. For each forbidden reflection, the corresponding background intensity was added to the calculated intensity. For all *Umweganregung* events, the Gaussian distribution (pseudo-Voigt parameter GL = 0) was used as the intensity profile function. The ψ shifts $\delta\psi$ between the

Table 2. *Background-corrected integrated intensities of permitted reflections I_{Bragg} and forbidden reflections I_{Umweg}* (counts min^{-1})

Observed $[\Delta\theta(\alpha_1)_{obs}]$ and calculated $[\Delta\theta(\alpha_1)_{calc}]$ half-widths of the Ag $K\alpha_1$ contribution defined in (2). Calculation performed with $\delta_p = 0.14°$, $\delta_s = 0.16°$, $r = 0.23$ μm, $\eta = 0.01°$, $\Delta\lambda/\lambda(\text{Ag } K\alpha_1) = 0.00048$ and $\Delta\lambda/\lambda(\text{Ag } K\alpha_2) = 0.00052$. $\delta\theta$ and $\delta\psi$ are the shifts between the experimental and calculated scans caused by the uncertainty of the orientation matrix.

Possible *hkl*	Forbidden *hkl*	θ (°) Ag $K\alpha_1$	$\delta\theta$ (°)	$\delta\psi$ (°)	I_{Bragg}	I_{Umweg}	$\Delta\theta(\alpha_1)_{obs}$ (°)	$\Delta\psi(\alpha_1)_{calc}$ (°)
002		6.51	−0.01		285829		0.18	0.17
$10\bar{2}$		9.55	0.01		49370		0.15	0.17
	003	9.79	0.01	−0.06		4815	0.17	0.17
110		12.12	0.02		115203		0.18	0.17
	$\bar{1}21$	12.56	−0.01	0.00		5705	0.18	0.17
$\bar{1}14$		14.89	0.02		12098		0.19	0.17
	$\bar{1}\bar{1}3$	15.67	0.02	−0.02		3333	0.18	0.17
	$\bar{1}1\bar{3}$	15.67	0.01	0.00		2772	0.19	0.17
	$03\bar{1}$	21.60	0.03	0.02		1109	0.18	0.17
032		22.39	0.02		12799		0.18	0.17
116		23.55	0.02		4685		0.18	0.17
	$0\bar{3}3$	23.67	−0.02	−0.06		749	0.18	0.17
$3\bar{1}\bar{5}$		25.34	0.02		3269		0.18	0.17
	$\bar{1}27$	26.66	0.00	0.06		253	0.18	0.18
008		26.95	−0.01		1200		0.18	0.18
314		29.49	−0.01		665		0.17	0.18
	$\bar{2}\bar{2}5$	30.43	0.02	−0.02		141	0.18	0.18
	$\bar{2}25$	30.43	−0.02	0.04		168	0.18	0.18
028		30.93	−0.02		145		0.19	0.18
$40\bar{4}$		32.36	−0.02		399		0.17	0.19
	$\bar{4}51$	33.95	0.01	0.02		122	0.18	0.18
0,0,10		34.51	−0.02		134		0.20	0.18
	$5\bar{4}\bar{3}$	35.52	0.03	0.06		108	0.18	0.18
051		37.50	−0.02		784		0.20	0.18
	$\bar{5}15$	38.58	–	0.12		32	–	0.18
420		39.90	−0.01		201		0.19	0.18
	$\bar{3}6\bar{3}$	40.73	–	−0.06		34	–	0.19
	$\bar{3}\bar{3}5$	43.68	–	−0.24		21	–	0.19
$1\bar{6}\bar{3}$		44.11	−0.02		301		0.19	0.19

experimental and calculated patterns caused by the uncertainty of the orientation matrix are given in Table 2. $\delta\psi$ is the only parameter that was fitted to the data.

It is obvious from Fig. 2 that, once the scale factor is known and the parameters δ_p, δ_s, η and r are obtained from previous work, *UMWEG*90 allows a reliable prediction of the magnitude of the intensity gain due to *Umweganregung* for all forbidden reflections of a particular sample. This demonstrates the utility of the concept introduced by Rossmanith (1992) for the evaluation not only of the *Umweganregung* patterns but also of the θ dependence of the *Umweganregung* intensities, which is mainly governed by the Lorentz factor L_θ corresponding to the θ rotation [see Rossmanith (1992) §II.*B*(*a*)2].

The agreement between the experimental and theoretical *Umweganregung* patterns is satisfactory, especially in view of the large number of lines contributing to the pattern (see the λ–ψ diagrams in Fig. 2), whose intensity is calculated correctly by *UMWEG*90 to be very small or even negligible. As was pointed out by Rossmanith *et al.* (1994), the deviations between measurement and calculation may be partly caused by the fact that absorption and extinction effects as well as the anisotropy of the mosaic structure of zinc (Rossmanith, 1977; Rossmanith *et al.*, 1994) are neglected in the actual version of *UMWEG*90.

Comparison of the intensities of forbidden and permitted reflections

In Table 2, the measured background-corrected integrated intensities of permitted Bragg reflections are compared with the intensities integrated over the ω–2θ scan of forbidden reflections caused by *Umweganregung* events. The intensities given in the seventh column of Table 2 were calculated with *UMWEG*90 using the same parameter set as before. Unlike the intensity values given in the 14 intensity-*versus*-ψ diagrams of Fig. 2, they represent the background-corrected *maximum* intensity in the respective 360° ψ scans and are therefore, in most cases, larger than the corresponding calculated and background-corrected intensities of the ψ range presented in Fig. 2.

It is obvious from Table 2 that even for small Bragg angles the maximum possible intensity of a forbidden reflection caused by multiple diffraction is significant, being comparable in magnitude with the neighbouring Bragg intensities for the high-order reflections.

Comparison of ω–2θ profiles of forbidden and permitted reflections

In Figs. 3 and 4, the ω–2θ scans of the permitted reflections $\bar{1}14$ and 116 are compared with ω–2θ scans of forbidden reflections having neighbouring Bragg angles.

The experimental peak intensities of the permitted reflections are composed of two contributions caused by Ag $K\alpha_1$ and Ag $K\alpha_2$ radiation with an intensity ratio $f(\alpha_1):f(\alpha_2) = 1:0.5$. It is obvious from Figs. 3(*a*) and 4(*a*) that the experimental profiles can be simulated by using for both contributions a modified Gaussian distribution function with constant intensity

$$I(\theta)_{\alpha_i} = I(\theta)_{\max} \qquad (1a)$$

in the range $\theta_{\alpha_i} - d\theta/2 < \theta < \theta_{\alpha_i} + d\theta/2$ and

$$I(\theta)_{\alpha_i} = I(\theta)_{\max} \exp\{-0.5[(\theta - \theta_{\alpha_i} \pm d\theta/2)/\sigma]^2\} \qquad (1b)$$

elsewhere. $d\psi$ is the width of the constant peak intensity region, $\theta_{\alpha i}$ (i = 1 or 2) is the experimental Bragg angle of the $K\alpha_1$ or $K\alpha_2$ radiation, $I(\theta)_{\max}$ is the maximum intensity of the theoretical distribution and σ is the standard deviation of the Gaussian distribution function. The half-width of this distribution is consequently given by

$$\Delta\theta(\alpha_i)_{\text{obs}} = (8 \ln 2)^{1/2}\sigma + d\theta. \qquad (2)$$

The theoretical profile of the composition is then

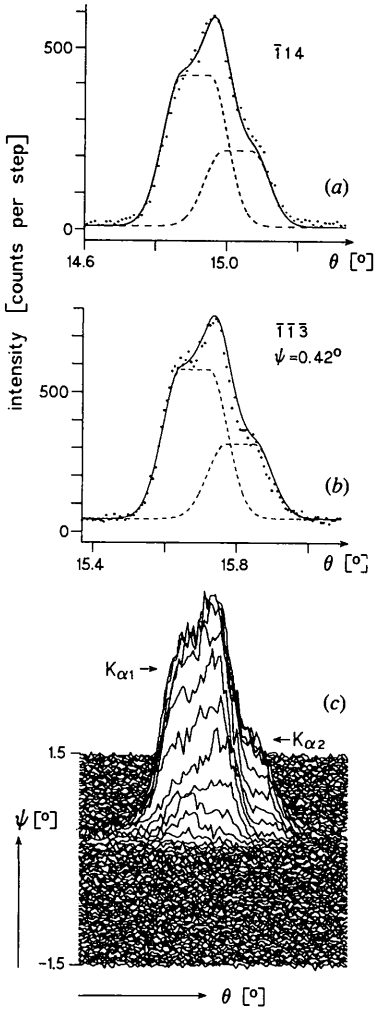

Fig. 3. Comparison of experimental (symbols) and theoretical ω–2θ profiles. Dashed lines: Ag $K\alpha_1$ and Ag $K\alpha_2$ profile contributions according to (1*a*) and (1*b*). Solid lines: theoretical profiles according to (3). (*a*) ω–2θ scan of the possible $\bar{1}14$ reflection. (*b*) ω–2θ scan of the forbidden $\bar{1}\bar{1}3$ reflection. (*c*) Three-dimensional plot of the ω–2θ–ψ scan of the $\bar{1}\bar{1}3$ reflection.

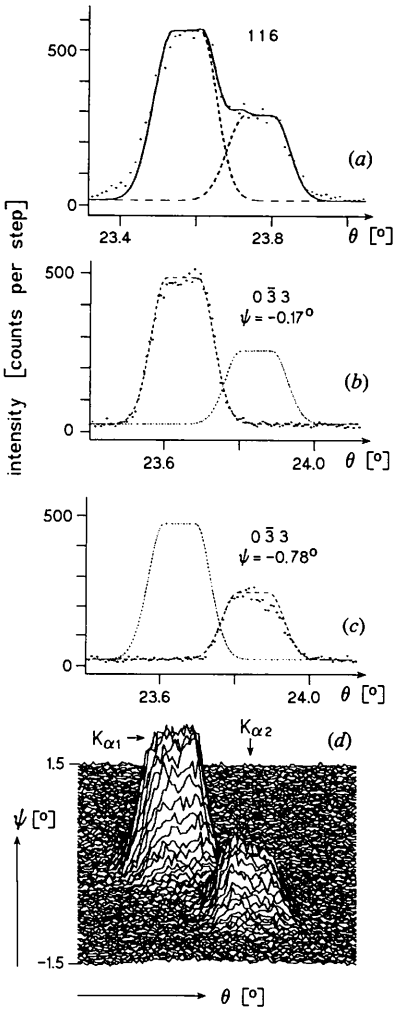

Fig. 4. Comparison of experimental (symbols) and theoretical ω–2θ profiles. Dashed lines: Ag $K\alpha_1$ and Ag $K\alpha_2$ profile contributions according to (1*a*) and (1*b*). Solid lines: theoretical profiles according to (3). (*a*) ω–2θ scan of the possible 116 reflection. (*b*) ω–2θ scan of the forbidden $0\bar{3}3$ reflection at $\psi = -0.17°$. (*c*) ω–2θ scan of the forbidden $0\bar{3}3$ reflection at $\psi = -0.78°$. (*d*) Three-dimensional plot of the ω–2θ–ψ scan of the $0\bar{3}3$ reflection.

obtained from

$$I(\theta) = \sum f(\alpha_i) I(\theta)_{\alpha_i} + \text{bgr}, \qquad (3)$$

where bgr is the background intensity. In Figs. 3(*a*) and 4(*a*), the $K\alpha_i$ contributions (1*a*) and (1*b*) are drawn as dashed lines and the compound profile according to (3) is shown as a solid line. The widths of the Ag $K\alpha_1$ contribution, $\Delta\theta(\alpha_1)_{\text{obs}}$, defined in (2) and obtained by fitting the theoretical profile (3) to the experimental ω–2θ scans of the 15 possible reflections are given in Table 2, together with the Bragg angles calculated for Ag $K\alpha_1$ and the θ shifts $\delta\theta$ between the experimental and calculated Bragg angles caused by the uncertainty of the lattice parameters.

In an analogous way, the widths of the $K\alpha_i$ contribution, $\Delta\theta(\alpha_i)_{\text{obs}}$, of the forbidden reflections were determined. It is obvious from the contour plots in combination with the upper λ–ψ diagrams in Fig. 2 that, in the case of the forbidden reflections, the ω–2θ intensity profile strongly depends on the difference between the ψ values of an *Umweganregung* event caused by the Ag $K\alpha_1$ and Ag $K\alpha_2$ radiation, respectively. The dependence of the azimuthal angle ψ on the wavelength λ for a particular *Umweganregung* event can easily be read off the λ–ψ diagrams shown in Fig. 2. The factors $f(\alpha_1)$ and $f(\alpha_2)$ in (3) may vary between zero and their maximum values 1 and 0.5, respectively, depending on the azimuthal angle of the ω–2θ scan under consideration. For example, in the case of the forbidden $1\bar{1}3$ reflection (Figs. 1, 3*b* and 3*c*), the two ψ values of the maximum *Umweganregung* intensities for the $0\bar{1}0/\bar{1}0\bar{3}$ event are nearly identical ($\psi_{K\alpha_1} = 0.40°$, $\psi_{K\alpha_2} = 0.44°$; see λ–ψ diagrams and contour plot in Fig. 2 and fifth and sixth columns of Table 1) whereas, in the case of the forbidden $0\bar{3}3$ reflection (Figs. 1, 2, 4*b*, 4*c* and 4*d* and Table 1), the ψ values of the $0\bar{1}2/0\bar{2}1$ event differ appreciably ($\psi_{K\alpha_1} = -0.17°$, $\psi_{K\alpha_2} = -0.80$). The experimental profile of the forbidden $1\bar{1}3$ reflection is therefore very similar to that of the possible $\bar{1}14$ reflection, whereas the $K\alpha_1$ and $K\alpha_2$ intensities are resolved in the case of the forbidden $0\bar{3}3$ reflection. Nevertheless, it can be deduced from Figs. 3 and 4 that, in both cases, the profiles of the Ag $K\alpha_i$ contributions defined in (1*b*) are nearly identical for the permitted and the forbidden reflections with neighbouring Bragg angles, even having the same range of constant intensity $d\theta$ in the maximum of the peak (see also Fig. 1). The compound profile according to (3), on the other hand, may differ appreciably for the permitted and forbidden reflections, not only because of the ψ difference of the two characteristic lines for *Umweganregung* reflections but also because of the overlapping of different *Umweganregung* peaks at a particular azimuthal angle ψ, as for example in the case of the forbidden $1\bar{2}\bar{7}$ reflection at $\psi = 0.34°$.

The widths of the Ag $K\alpha_1$ contribution to the intensity profile of the permitted and forbidden reflections, $\Delta\theta(\alpha_i)_{\text{calc}}$, given in the ninth column of Table 2 were calculated with *UMWEG*90.* The calculation was performed using the same parameter set as before. These calculated widths agree very well with the observed widths $\Delta\theta(\alpha_i)_{\text{obs}}$, given in the eighth column, confirming the statement given by Rossmanith [1992, §II.*B*(*a*)2]: 'Because of the dominant influence of the divergence δ_p on the peak width $\Delta\theta_{\text{Umweg}}$, if a conventional X-ray tube is used as source of the incident beam, the peak widths $\Delta\theta_{\text{Umweg}}$ are nearly equal in magnitude for all *Umweganregung* peaks in the θ–2θ–ψ–scan of the primary reflection and are almost equal to the peak width $\Delta\theta_{\text{prim}}$'. These facts are evident from the contour plots given in Fig. 2 and from Table 2.

Because of the equivalent relation in reciprocal space between the width of an ω–2θ scan and a spot size on a film for permitted and forbidden reflections, the statement given in standard textbooks, that the profiles of *Umweganregung* events are much sharper than those of permitted reflections and have a different shape, is questioned or even disproved. It is clear from this result that Lipson & Cochran's (1957) statement that 'the double reflections are formed by reflection of truly parallel rays' is incorrect.

Comparison of $\Delta\theta$ and $\Delta\psi$

It can easily be read from the contour plots given in Fig. 2 that, whereas the measured widths of the characteristic lines $\Delta\theta(\alpha_i)$ are obviously constant for different *Umweganregung* events within one particular ω–2θ–ψ scan and nearly constant for the different ω–2θ–ψ scans, the widths $\Delta\psi(\alpha_i)$ of the various *Umweganregung* events differ appreciably and are in most cases much larger than $\Delta\theta(\alpha_i)$. This behaviour of the widths $\Delta\theta(\alpha_i)$ and $\Delta\psi(\alpha_i)$ as well as the relative intensities of the peaks within one *Umweganregung* pattern and between different *Umweganregung* patterns are predicted satisfactorily with *UMWEG*90.

In a recent paper, Mathieson (1994) questioned the formulas used in *UMWEG*90 and pointed out that 'the modes of combination of components' in the new peak-width formula proposed by Rossmanith (1992, 1993*a*,*b*) 'differ significantly from those associated with earlier published work'. In deducing the peak width in reciprocal space, the author of *UMWEG*90 was aware of this fact.

In Table 3, the contributions to the full widths at half-maxima (FWHMs) $\Delta\theta(\alpha_i)$ and $\Delta\psi(\alpha_i)$ caused by the parameters $\Delta\lambda/\lambda$, δ_p, δ_s, r and η and the dependence on the relative peak intensities calculated with *UMWEG*90 are given for the $0\bar{1}0/\bar{1}0\bar{3}$ *Umweganregung* event of the forbidden reflections $1\bar{1}3$ and for the event $0\bar{1}2/0\bar{2}1$ of the forbidden $0\bar{3}3$ reflection. It is clear from these two

* As was pointed out by Rossmanith (1994), the relation $\varepsilon = 1/r$ given by Rossmanith (1992) has to be replaced by $\varepsilon = 0.235/r$.

Table 3. *The contributions to the FWHMs $\Delta\theta(\alpha_1)_{calc}$ and $\Delta\psi(\alpha_1)_{calc}$ caused by $\Delta\lambda/\lambda$, δ, r and η; dependence of the relative intensity on the width*

					$\bar{1}\bar{1}\bar{3}$ / $0\bar{1}0/\bar{1}0\bar{3}$			$0\bar{3}\bar{3}$ / $0\bar{1}2/0\bar{2}1$		
$\Delta\lambda/\lambda$	r (μm)	η (°)	δ_p (°)	δ_s (°)	$\Delta\theta(\alpha_1)$ (°)	$\Delta\psi(\alpha_1)$ (°)	I (%)	$\Delta\theta(\alpha_1)$ (°)	$\Delta\psi(\alpha_1)$ (°)	I (%)
0	0.23	0	0	0	0.01	0.04	68	0.01	0.11	100
0.00048	∞	0	0	0	0.01	0.01	80	0.01	0.05	100
0.00048	0.23	0	0	0	0.02	0.04	70	0.02	0.13	100
0	∞	0	0.14	0	0.14	0.0	70	0.14	0.0	100
0	∞	0	0	0.16	0	0.17	52	0	0.18	100
0	∞	0.01	0	0	0.01	0.02	52	0.01	0.08	100
0.00048	0.23	0.01	0.14	0.16	0.17	0.23	56	0.17	0.39	100

examples that $\Delta\theta(\alpha_i)$ given in the last line of Table 3 can approximately be calculated by the sum of the individual contributions caused by $\Delta\lambda/\lambda$, δ_p, r and η. No such simple relation holds true for $\Delta\psi(\alpha_i)$. Furthermore, comparison of the widths $\Delta\psi(\alpha_1)$ of the two examples given in Table 3 shows that the magnitude of the contributions caused by the four parameters strongly depends on the *Umweganregung* event under consideration, *i.e.* on the locus at which the corresponding reciprocal-lattice point crosses the Ewald sphere. It is also clear from the table that the relative intensities within an ω–2θ–ψ scan strongly depend on the widths of the peaks. (In the case of the strongest *Umweganregung* peak, $I = 100\%$, the relative intensity is of course constant and the corresponding calculated scaled 'absolute' intensity depicted in Fig. 2 is width dependent.) The widths as well as the heights of the intensity profiles are therefore strongly dependent on the 'modes of combination of components'.

The very good results obtained with *UMWEG*90, presented in this and the previous papers, and the consistency of the results for single and double diffraction (permitted and forbidden reflections) confirm the applicability of the new concept for the calculation of the peak width proposed by Rossmanith (1992, 1993*a*,*b*) and justify its use.

On the other hand, there is no doubt that the expressions used in the actual version of the program *UMWEG*90 are approximations capable of improvement. More detailed answers on the criticisms by Mathieson will be given in a forthcoming paper.

Discussion

Once more it has been shown, in this paper, that the concept for the calculation of peak profiles, *i.e.* the calculation of the height and width of the intensity distributions, introduced by Rossmanith (1992) results in very good or at least satisfactory agreement between experiment and theory.

Bearing in mind that, in the case of a small wavelength-to-cell-parameter ratio many thousands of particular profiles have to be added together for the simulation of a ψ scan, no computer-time-consuming algorithm such as convolution (Alexander & Smith, 1962) can be used for calculation. The main advantages of the approach given by Rossmanith (1992) are therefore its simplicity and its successful applicability to X-ray tubes as well as to synchrotron radiation (Rossmanith, 1993*a*,*b*; Rossmanith, Werner, Kumpat, Ulrich & Eichhorn, 1993), to single crystals as well as to powders (Rossmanith, 1994) and to single diffraction as well as to multiple diffraction (Rossmanith *et al.*, 1994).

References

ALEXANDER, K. E. & SMITH, G. S. (1962). *Acta Cryst.* **15**, 983–1004.

AZAROFF, L. V. (1968). *Elements of X-ray Crystallography*. New York: McGraw-Hill.

COMPTON, A. H. & ALLISON, S. K. (1935). *X-rays in Theory and Experiment*. Princeton, New Jersey: van Nostrand.

LIPSON, H. & COCHRAN, W. (1957). *The Determination of Crystal Structures. The Crystalline State*, Vol. III, edited by L. BRAGG. London: G. Bell and Sons.

MATHIESON, A. MCL. (1994). *Acta Cryst.* A**50**, 123–126.

ROSSMANITH, E. (1977). *Acta Cryst.* A**33**, 593–601.

ROSSMANITH, E. (1992). *Acta Cryst.* A**48**, 596–610.

ROSSMANITH, E. (1993*a*). *Acta Cryst.* A**49**, 80–91.

ROSSMANITH, E. (1993*b*). *J. Appl. Cryst.* **26**, 753–755.

ROSSMANITH, E. (1994). *Acta Cryst.* A**50**, 63–68.

ROSSMANITH, E., ADIWIDJAJA, G., ECK, J., KUMPAT, G. & ULRICH, G. (1994). *J. Appl. Cryst.* **27**, 510–516.

ROSSMANITH, E., KUMPAT, G. & SCHULZ, A. (1990). *J. Appl. Cryst.* **23**, 99–104.

ROSSMANITH, E., WERNER, M., KUMPAT, G., ULRICH, G. & EICHHORN, K. (1993). *J. Appl. Cryst.* **26**, 756–762.